

# **A map and a pipe: a new approach to characterizing erosion-corrosion regimes of Fe in three dimensions using CFD modelling**

**M.M. Stack<sup>1</sup>, S.M. Abdelrahman<sup>2</sup> and B.D. Jana<sup>3</sup>**

*University of Strathclyde,*

*James Weir Building*

*75 Montrose St.,*

*Glasgow, G1 1XJ, UK*

*<sup>1</sup>Corresponding author*

*<sup>1</sup>University of Strathclyde, UK E-mail: [margaret.stack@strath.ac.uk](mailto:margaret.stack@strath.ac.uk)*

*<sup>2</sup>University of Strathclyde, UK, [s.m.abdelrahman@strath.ac.uk](mailto:s.m.abdelrahman@strath.ac.uk)*

*<sup>3</sup>University of Strathclyde, UK, [buddhadev.jana@corusgroup.com](mailto:buddhadev.jana@corusgroup.com)*

## **Abstract**

In studies of erosion-corrosion, much work has been carried out in recent years to identify regimes of behaviour. Such regimes describe the transition between the erosion and corrosion dominated mechanisms. They can also be used, by assigning various criteria, to identify other regimes of behaviour such as extent of “synergy/antagonism” in the process, so-called “additive” behaviour and the extent of wastage.

Despite this work, there has been very little effort to combine the concept of the two dimensional erosion-corrosion map with CFD modelling approaches, in which the characteristics of the fluid are accounted for in the regime description. This means that extrapolation of such maps in two dimensions to a three dimensional real surface presents some difficulties. However, it is these surfaces that corrosion engineers

are required to tailor, either through modification of the material composition, the surface or the process parameters, for optimum erosion-corrosion resistance.

In this paper, a methodology is generated to combine the concepts of CFD modelling, and the erosion-corrosion regime map for a specific geometry and for a range of pure metals in descending order in the Galvanic series. The changes in regimes are presented as a function of variation in the erosion and corrosion variables i.e. particle size, hardness and solution pH. Erosion-corrosion regimes are presented, based on the model results, showing the wide range of mechanistic and wastage mechanisms possible over the component surface.

**Keywords:** Erosion-Corrosion, CFD Modelling, Regimes, Maps

## 1. Introduction

There have been several attempts at characterizing erosion-corrosion interactions reported in the literature in recent years [1-5]. These include theoretical and experimental methodologies to describe the erosion-corrosion interactions. Various regimes descriptions have been employed in order to distinguish between the relative contributions of erosion and corrosion and, whether the effect of corrosion on erosion enhances the overall wastage rate in a so-called “synergistic” manner, or impedes it in an antagonistic manner [1-4].

Several recent studies have used CFD (Computational Fluid Dynamics) simulation to predict erosive wear in “real life” components [5]. Other work [6] has used pre-determined experimental data [7] to test the predictions of the latter model for the erosion-corrosion on the inner surfaces of a pipe. A further approach [8, 9] has used CFD to predict wear due to erosion-corrosion on other real-life systems.

In dry conditions, erosion-corrosion simulations were carried out [10] to model the erosion of an alumina oxide scale on an aluminium alloy substrate and to investigate the multiple impact of particles on a single site. This revealed that the crack formation due to tensile failure and shear stress could be simulated and predicted. A further erosion-corrosion study in aqueous conditions involved a finite difference method [11] to estimate the corrosion rates using knowledge of the concentration of ions in the near wall area. This revealed that changes in oxygen concentration will also increase the pH level and thus the amount of Fe ions released from the pipe surface.

CFD [12] was used to investigate the relationship between shear stress of the oblique impact flow and the dissolution of the aluminium oxide layer. Other work [13] has found experimental agreement with model predictions for erosion-corrosion of a 304 L steel in aqueous conditions. Hence, there has been significant activity in CFD modelling of erosion-corrosion, both in dry and aqueous conditions in the past five years.

Despite such studies, there has been no work carried out to combine the erosion-corrosion mapping approach with CFD simulations of the wastage process. This paper addresses this issue by combining various erosion models in a CFD analysis with those for aqueous corrosion. Furthermore, these models are incorporated in a simulation of a multiphase flow environment using the Dispersed Particle Method (DPM) techniques for solid particle tracking. The results for “mapping the pipe” present a new technique for characterizing erosion-corrosion on real pipes, thereby introducing an important step-change in the interpretation and use of erosion-corrosion mapping approaches to date.

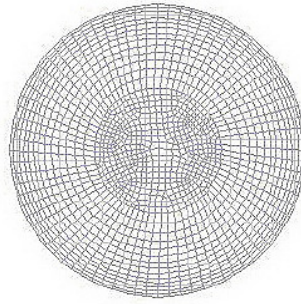


Figure 1: Diagram of front view of mesh generated at inlet of component.

## 2. Methodology

### 2.1. Slurry Flow Modelling

The following are the various steps in the model development.

- (i) A dilute slurry flow of water-alumina sand particles, of size  $10^{-3}$ [m] and volume fraction of 0.1, was ingested through a pipe bend inlet with bore diameter  $D$  equal to 0.078 [m] and  $R_c D^{-1}$  ratio of 1.2.
- (ii) The CFD simulations were generated by FLUENT ver.6.3 [14], which uses a finite element based finite volume method to solve the flow governing equations. Table 1 summarizes the equations and operating and boundary conditions used in this study while table 2 lists the mechanical and physical properties for the slurry and target material. Figure 1 illustrates the mesh at the inlet which was generated and used for the study.
- (iii) A structured grid was generated in the near wall region together with a unstructured grid in the bulk flow region. The imbalance between the mass flow rate in the exit boundary compared to that in the inlet was computed (to ensure mass continuity) and found to be  $1.144 \times 10^{-5}$ [kg s<sup>-1</sup>].
- (iv) To validate the CFD analysis, a comparison with the case study [15] was carried out as shown in table 3. The validation exercise was carried out for SS304L stainless steel alloy using the Forder erosion model [16].
- (v) The results in the current work were simulated for mild steel using Sundararajan's second model [17].

### 2.2. Erosion models

As stated above, the models used include that of Forder's erosion model [16] given as:

where

$$\dot{W} = \frac{100 r_p^3}{2 \sqrt{29}} \left( \frac{V_p}{C_k} \right)^n \sin(2\alpha) \sqrt{\sin \alpha} + \frac{m_p}{2 E_f} (V_p \sin \alpha - D_k)^2 \quad (1)$$

$$C_k = \sqrt{\frac{3 \sigma R_f^{0.6}}{\rho_p}} \quad (2)$$

and

$$D_k = \frac{\pi^2}{2\sqrt{10}} (1.59 Y)^{2.5} \left(\frac{R_f}{\rho_t}\right)^{0.5} \left[ \frac{(1 - \nu_p^2)}{E_t} + \frac{(1 - \nu_t^2)}{E_p} \right]^2 \quad (3)$$

The second model of Sundararajan [17] is divided into two expressions, one for localised deformation at the impact point, while the other accounts for the ductile cutting mechanism during the impact [17] i.e.

$$Er_{def} = \frac{5.5 \times 10^{-2}}{(T_m - 436)^{0.75}} \frac{2^{n_c} f_t (V_p \sin \alpha)^2 (1 - e_n^2)}{n_c C_p} \quad (4)$$

$$Er_{cut} = \frac{5.5 \times 10^{-2}}{(T_m - 436)^{0.75}} \frac{(n_c + 1) \left(\frac{\mu_f}{\mu_{fc}}\right) \left(2 - \frac{\mu_f}{\mu_{fc}}\right) (V_p \cos \alpha)^2}{2^{(2-n_c)} (1 + \lambda) n_c C_p} \quad (5)$$

where:

$$\mu_{fc} = \frac{1}{(1 + \lambda) (1 + e_n) \tan \alpha} \quad (6)$$

The coefficient of restitution  $e$  can be estimated either by relating the energy dissipated during the impact with the mechanical properties of the target and impact velocity [18]. This is valid only for normal impact.

$$e_n = \frac{1.36 H_s^{0.625}}{E_e^{0.5} \rho_p^{0.125} V_p^{0.25}} \quad (7)$$

or it can be related to the impact angle through a semi-empirical relation [16]:

$$e_n = 0.988 - 0.78 \alpha + 0.19 \alpha^2 - 0.024 \alpha^3 + 0.027 \alpha^4 \quad (8)$$

$$e_t = 1.0 - 0.78 \alpha + 0.84 \alpha^2 - 0.21 \alpha^3 + 0.028 \alpha^4 - 0.022 \alpha^5 \quad (9)$$

For consistency with corrosion rate calculations, erosion rates are converted to  $[\text{kg m}^{-2} \text{s}^{-1}]$ .

### 2.3. Corrosion models

#### 2.3.1. Active corrosion model

Assuming that the corrosion reaction is activation controlled, the dissolution current density is given by the Butler-Volmer equation [19]:

$$i = i_o \left[ \exp\left(\frac{2.303 \Delta E}{b_a}\right) - \exp\left(\frac{-2.303 \Delta E}{b_c}\right) \right] \quad (10)$$

where the over-potential is defined as:

$$\Delta E = E_{app} - E_{rev} \quad (11)$$

the corrosion rate is therefore given by

$$K_c = \frac{i M_{Fe}}{z_m F} \quad (12)$$

#### 2.3.2. Repassivation model

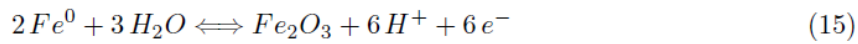
An expression for the corrosion rate under passivation condition has been introduced [20] and is currently modified to include the effect of the oblique impact [21].

$$\Delta K_c = \pi k_2 h \rho_f d_p^2 \left[ \frac{\rho_p (1 - e_n^2)}{6 H_s} \right]^{0.5} \frac{c_p (V_p \sin(\alpha))^2}{m_p} \quad (13)$$

where  $h$  can be assumed to be related to the over-potential of the passivation [22]:

$$h = h_o + 3 \times 10^{-9} (E - E_{pas}) \quad (14)$$

2.3.3. *Determination of passivation potential* based on the simplified Pourbaix diagram [23], Figure 2 shows the Pourbaix diagram for pure Fe. The passivation potential  $E_{pas}$  can be determined from the intersection of the operating pH.



The equation of this line can be given by [24].

The passivation potential is expressed in [V] with respect to standard calomel electrode (SCE).

$$E_{pas} = 1.08 - 0.177 pH - 0.245 \quad (16)$$

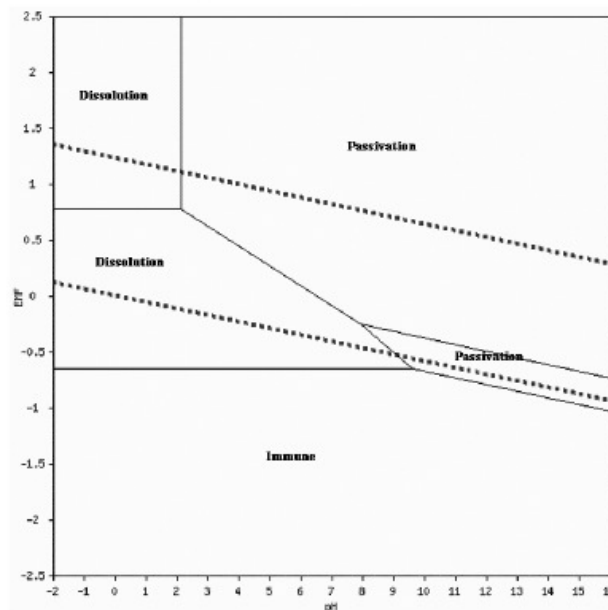


Figure 2: Pourbaix diagram for Fe.

#### 2.4. Erosion-corrosion mapping

The total wear can be estimated as the sum of the erosion and corrosion rates i.e.

$$K_t = K_e + K_c \quad (17)$$

where

$$K_e = K_{eo} + \Delta K_e \quad (18)$$

and

$$K_c = K_{co} + \Delta K_c \quad (19)$$

In the active region, the erosion enhanced corrosion  $\Delta K_c$  and corrosion enhanced erosion  $\Delta K_e$  are neglected while in passive region, the pure corrosion is much lower than the erosion enhanced corrosion. Hence, in the active region, the total wear is given by:

$$K_t = K_{eo} + K_{co} \quad (20)$$

and in passive region

$$K_t = K_{eo} + \Delta K_c \quad (21)$$

The regime boundaries needed for constructing the regime maps on the interior surfaces of the pipe are defined by the ratio  $K_c/K_e$ . and are used to determine the transition regimes at a given applied pH and applied potential.

$$\frac{K_c}{K_e} < 0.1 \quad (\text{erosion dominated}) \quad (22)$$

$$0.1 \leq \frac{K_c}{K_e} < 1 \quad (\text{erosion - corrosion}) \quad (23)$$

$$1 \leq \frac{K_c}{K_e} < 10 \quad (\text{corrosion - erosion}) \quad (24)$$

$$\frac{K_c}{K_e} \geq 10 \quad (\text{corrosion dominated}) \quad (25)$$

The wastage maps boundaries are set to give the transition regions between low, medium and high wastage. These are set as low wastage i.e. less or equal to 1 [mm year<sup>-1</sup>], medium

wastage i.e. between 1-10 [mm year<sup>-1</sup>] and high wastage i.e. greater or equal to 10 [mm year<sup>-1</sup>]. [Units are converted from [kg m<sup>-2</sup>s<sup>-1</sup>] to [mm year<sup>-1</sup>] in the model].

### 3. Results

The simulation commenced by using a single phase CFD run using FLUENT software and then injecting the particles uniformly at the inlet by using DPM method. A sample of 1655 particles of 10<sup>-3</sup> [m] diameter was injected. Each impact with the walls of the pipe triggered a UDF (User Defined Function) to calculate the erosion and corrosion rates. All figures incorporate a blue area indicating that there was no erosion occurring on this section of the component in order to distinguish it from the areas of the component where impacts are observed.

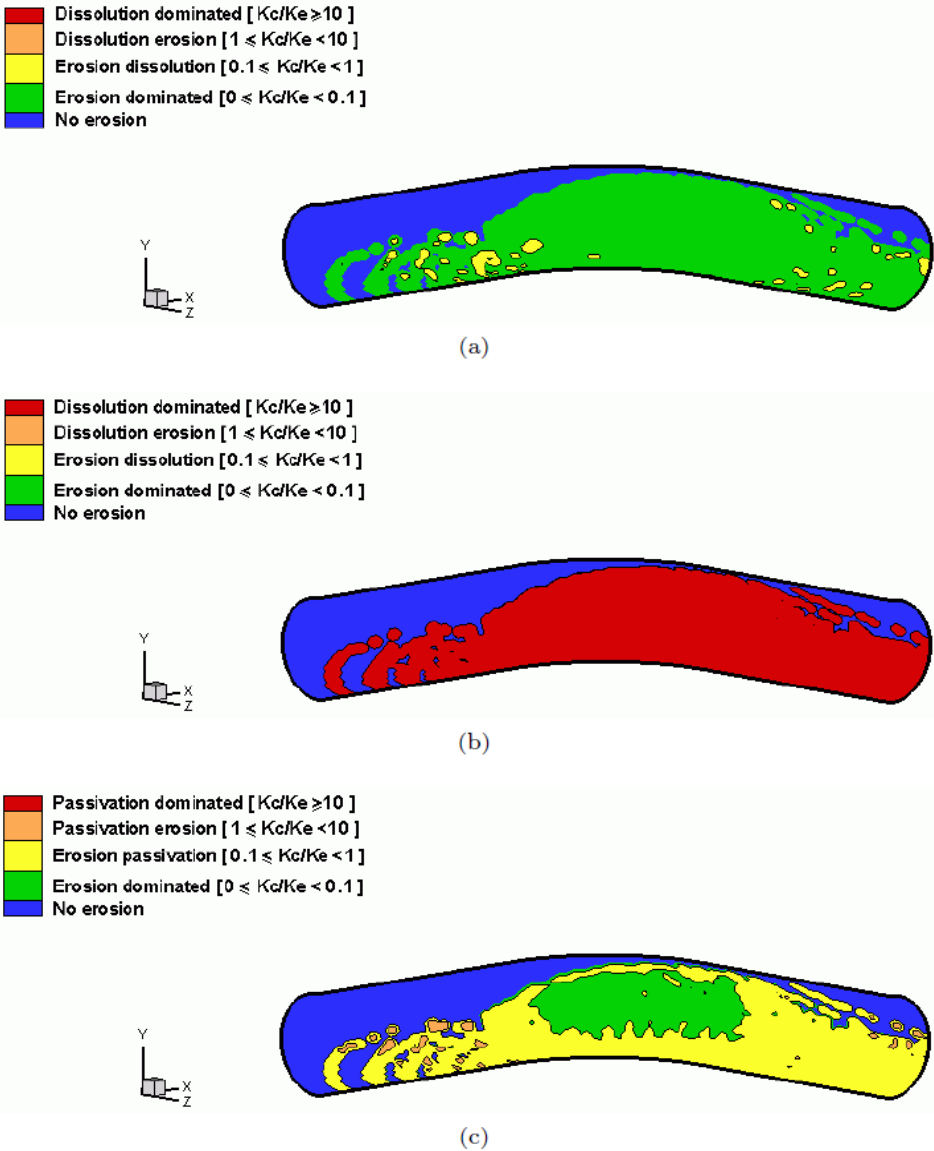


Figure 3: Erosion-corrosion maps for Fe component at  $V = -0.6 V$  [SCE] and pH: (a) 5 (b) 7

(c) 9.

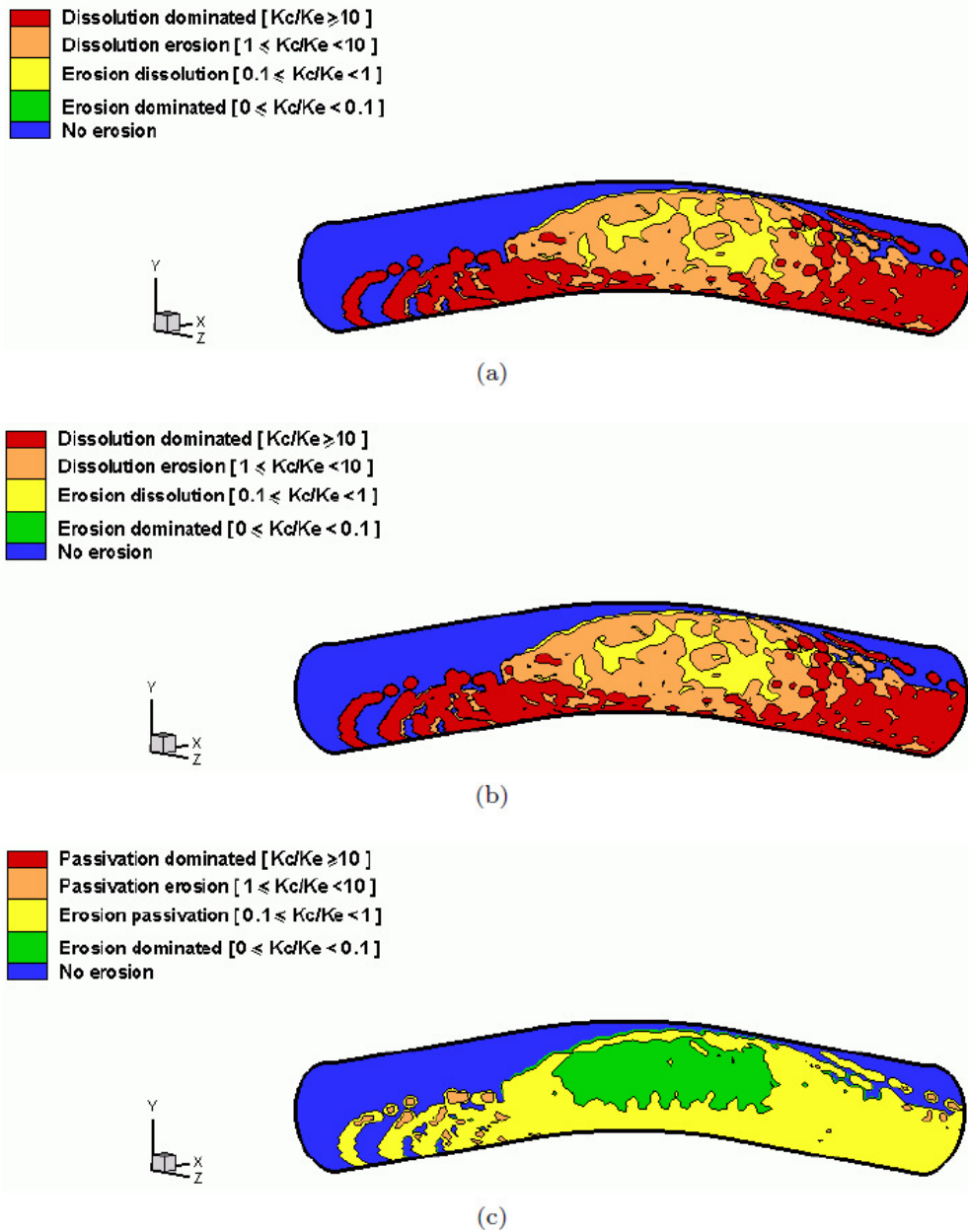


Figure 4: Erosion-corrosion maps for Fe component at  $pH = 7$  and applied potential [V][SCE]: (a)  $-0.75$  (b)  $-0.5$  (c)  $-0.25$ .

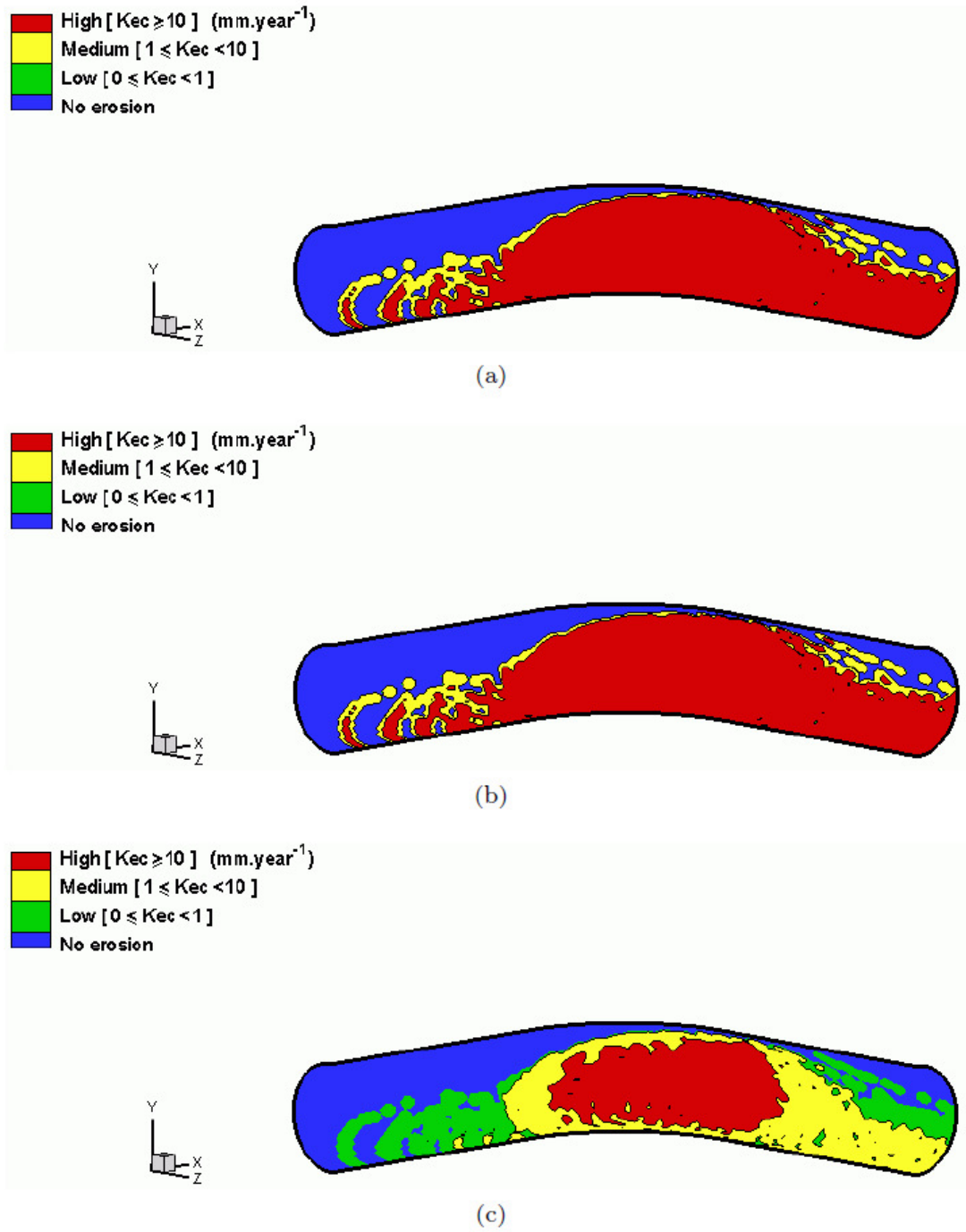


Figure 5: Wastage maps for Fe component at  $V = -0.6 \text{ V[SCE]}$  and pH: (a) 5 (b) 7 (c) 9.

### 3. Results

#### 3.1. Effect of pH on the erosion-corrosion map

The results, Fig. 3, showed that at pH 5 and 7, the erosion-corrosion regime pattern for Fe consisted mainly of dissolution and dissolution – erosion dominated behaviour. However, at pH 9, there was a change in the pattern of wastage, with the predominant erosion-corrosion regime for the component being erosion-passivation. This can be compared to the Pourbaix diagram for Fe, Fig. 2, with Fe passivating at high pH values.

#### 3.2. Effect of applied potential on the erosion-corrosion transition boundaries.

Changes in applied potential in the positive direction, Fig. 4 (a-b), from -0.75 V (SCE), to -0.5 V (SCE), indicated there was very little evidence of corrosion affecting the process at the lower potentials. Increase in applied potential, to -0.5 V (SCE) however, effected a significant change in the erosion-corrosion regime, with the component now being dominated by dissolution. At the higher potentials, by contrast, the erosion-corrosion regime was mainly erosion-passivation, Fig.4 (c)

#### 3.3. Wastage maps generated by simulation results at various pH values

The wastage maps, Fig. 5(a-b), indicated, consistent with the regime maps, Fig. 3(a-b), that there were similar wastage regimes predominating at pH 5 and 7. The high wastage rates over the component were attributed to the dissolution dominated regime which predominated. At higher pH values, Fig. 5 (c), at pH 9, there was a change in wastage mechanism with the high wastage regime mainly predominating over the middle of the component.

### 4. Discussion

It is clear from the results that the stability regimes for Fe as identified on the Pourbaix diagrams, Fig. 2, determine the erosion-corrosion regimes, Fig. 3-5.. The change in regime from dissolution affected behaviour at pH 5 and 7 to in turn passivation affected behaviour at pH 9, is consistent with the changes in the corrosion stability region on the Pourbaix diagram, Fig. 2. Moreover, the variation in distribution of particle impacts and velocities over the surface also have an effect on the erosion-corrosion regime, particularly in the passive region of the Pourbaix diagram, where particle re-passivation rates between impacts will result in high wastage rates, Fig. 3(c), Fig. 4(c).

The change in electrochemical potential in the positive direction, Fig. 4, shows significant shifts in the erosion-corrosion regimes over the surface. Increases in the potential in a positive direction can modify the corrosion regime and in so doing change the erosion response as, in the passive region, this will be greater than in the active region due to re-passivation, as indicated above.

For the purpose of the model, a blue area has been incorporated to distinguish the location of the component where no erosion is taking place. Depending on the corrosion conditions, this may be subject to corrosion. However, in this work, it was though important to highlight this region independently in the CFD simulation.

Various developments in mapping methodologies in two dimensions [24-28] have concentrated on assessing the changes in erosion-corrosion regime according to the position on the Galvanic series, and considering the erosion-corrosion regimes for composite materials where synergistic erosion-corrosion effects may be high. Other work has assessed the effect of oxygen concentration on the erosion-corrosion behaviour [29]. At present the effect of corrosion on the mechanical properties of the material is not considered for simplicity in the existing model although it is acknowledged that this may be a very significant in the overall wastage rate. Further work will be to consider these factors in the three dimensional CFD simulations.

Hence, the results indicate that it is possible to superimpose erosion-corrosion regimes on three dimensional component surfaces such as pipes. This is a new development in research in erosion-corrosion mapping and three dimensional modelling should enable more precise prediction of erosion-corrosion rates according to various geometries. Many important applications of this approach are envisaged over the wider tribo-corrosion area.

## 5. Conclusions

- (i) A method to superimpose the erosion-corrosion maps on the surfaces of Fe components has been developed using CFD analysis.
- (ii) The results have shown that it is possible to identify erosion-corrosion regimes in 3-dimensional applications.
- (iii) Such a technique offers great promise in transferring the existing tribo-corrosion mapping methodologies to many other processes where tribology interacts with corrosion.

## 6. References

- [1] Stack, M. M., Corlett, N. and Zhou, S. (1997) A methodology for the construction of the erosion-corrosion map in aqueous environments. *Wear*. **203** 474-488.
- [2] Stack, M. M. and Pungwiwat, N. (2002) Particulate erosion-corrosion of Al in aqueous conditions: some perspectives on pH effects on the erosion-corrosion map. *Tribology International*. **35** 651-660.
- [3] Jana, B. D. and Stack, M. M. (2005) Modelling impact angle effects on erosion-corrosion of pure metals: Construction of materials performance maps. *Wear*. **259**(1-6) 243-255.
- [4] Stack, M. M. and Abd El Badia, T. M. (2006) On the construction of erosion-corrosion maps for WC/Co-Cr-based coatings in aqueous conditions. *Wear*. **261**(11-12) 1181-1190.
- [5] Keating, A. and Nesic, S. (1999) Prediction of Two-phase Erosion-corrosion in Bends. Second International Conference on CFD in the Minerals and Process Industries, CSIRO pp. 229-236.
- [6] Davis, C. and Frawley, P. (2009) Modelling of erosion-corrosion in practical geometries. *Corrosion Science*. **51**(4) 769-775.
- [7] Founti, M. and Klipfel, A. (1998) Experimental and computational investigations of nearly dense two-phase sudden expansion flows. *Experimental Thermal and Fluid Science*. **17**(1-2) 27-36.
- [8] Ferng, Y. M., Ma, Y. P., Ma, K. T. and Chung, N. M. (1999) A new approach for

- investigation of erosion-corrosion using local flow models. *Corrosion*. **55**(4) 332-342.
- [9] Ferng, Y. M., Ma, Y. P. and Chung, N. M. (2000) Application of local flow models in predicting distributions of erosion-corrosion locations. *Corrosion*. **56**(2) 116-126.
- [10] Griffin, D., Daadbin, A. and Datta, S. (2004) The development of a three-dimensional finite element model for solid particle erosion on an alumina scale/MA956 substrate. *Wear*. **256**(9-10) 900-906.
- [11] Naser, G. and Karney, B. (2007) A 2-d transient multicomponent simulation model: Application to pipe wall corrosion. *Journal of Hydro-Environment Research*. **1** 56-69.
- [12] Xu, L. Y. and Cheng, Y. F. (2008) Electrochemical characterization and CFD simulation of flow-assisted corrosion of aluminum alloy in ethylene glycol-water solution. *Corrosion Science*. **50**(7) 2094-2100.
- [13] Wood, R. J. K., Jones, T. F., Ganeshalingam, J. and Miles, N. J. (2004) Comparison of predicted and experimental erosion estimates in slurry ducts. *Wear*. **256**(9-10) 937-947.
- [14] FLUENT, I. (2006) Ttile., Lebanon, NH, USA.
- [15] Wood, R. J. K. and Jones, T. F. (2003) Investigations of sand-water induced erosive wear of AISI 304L stainless steel pipes by pilot-scale and laboratory-scale testing. *Wear*. **255** 206-218.
- [16] Forder, A., Thew, M. and Harrison, D. (1998) A numerical investigation of solid particle erosion experienced within oilfield control valves. *Wear*. **216**(2) 184-193.
- [17] Sundararajan, G. (1991) A comprehensive model for the solid particle erosion of ductile materials, *Wear*. **149**(1-2) 111-127.
- [18] Stack, M. M., Corlett, N. and Zhou, S. (1998) Some thoughts on the effect of elastic rebounds on the boundaries of the aqueous erosion-corrosion map. *Wear*. **214**(2) 175-185.
- [19] Marcus, P. (2002) *Corrosion Mechanisms in Theory and Practice* Marcel Dekker, Inc., New York.
- [20] Stack, M. M., Corlett, N. and Zhou, S. (1996) Construction of erosion-corrosion maps for erosion in aqueous slurries. *Materials Science and Technology*. **12**(8) 662-672.
- [21] Abdelrahman, S. M. and Stack, M. M. (2009) Some reflections on a model to predict the erosion rate of the passive film on pure materials. Thirteenth International Conference on Aerospace Science and Aviation Technology, ASAT pp. In press.
- [22] Graham, M. J., Bardwell, J. A., Sproule, G. I., Mitchell, D. F. and Macdougall, B. R. (1993), The growth and stability of passive films. *Corrosion Science*. **35**(1-4) 13-18.
- [23] Pourbaix, M. (1966) *Atlas of Electrochemical Equilibria in Aqueous Solutions* Pergamon Press, Oxford, New York.
- [24] Stack, M. M. and Jana, B. D. (2004) Modelling particulate erosion-corrosion in aqueous slurries: some views on the construction of erosion-corrosion maps for a range of pure metals. *Wear*. **256**(9-10) 986-1004.
- [25] Stack, M. M. and Bray, L. (1995) Interpretation of wastage mechanisms of materials exposed to elevated temperature erosion using erosion-corrosion maps and computer graphics, *Wear*. **186**(1) 273-283.
- [26] Stack, M. M., Corlett, N. and Turgoose, S. (1999) Some recent advances in the

- development of theoretical approaches for the construction of erosion-corrosion maps in aqueous conditions. *Wear*. **233** 535-541.
- [27] Stack, M. M. and El-Badia, T. M. A. (2008) Some comments on mapping the combined effects of slurry concentration, impact velocity and electrochemical potential on the erosion-corrosion of WC/Co-Cr coatings. *Wear*. **264**(9-10) 826-837.
- [28] Stack, M. M., Antonov, M. M. and Hussainova, I. (2006) Some views on the erosion-corrosion response of bulk chromium carbide based cermets. *Journal of Physics D-Applied Physics*. **39**(15) 3165-3174.
- [29] Liu, J. J., Lin, Y. Z. and Li, X. Y. (2008) Numerical simulation for carbon steel flow-induced corrosion in high-velocity flow seawater. *Anti-Corrosion Methods and Materials*. **55**(2) 66-72.

**Tables:***Table 1: CFD modelling equations, operating and boundary conditions.*

<b>Model parameter</b>	<b>Water</b>	<b>Alumina sand</b>
<b>Solver equations</b>	Navier-Stokes	DPM
<b>Turbulence</b>	Standard k- $\epsilon$	
<b>Wall treatment</b>	Standard wall function	
<b>Coupling</b>		Two-way coupling
<b>Operating conditions</b>	Ambient	
<b>Inlet velocity [<math>\text{m s}^{-1}</math>]</b>	3.0	3.0

*Table 2: Physical and mechanical properties for the slurry and target material.*

<b>Model parameter</b>	<b>Fluid (Water)</b>	<b>Sand (alumina)</b>	<b>Target (mild steel)</b>
<b>Density [<math>\text{kg m}^{-3}</math>]</b>	998		7850
<b>Particle size [m]</b>		$10^{-3}$	
<b>Mass flow rate [<math>\text{kg s}^{-1}</math>]</b>	14.3	3.827	

*Table 3: Comparison between the current study and experimental and simulation of other workers [15]*

<b>Model parameter</b>	<b>Experimental [15]</b>	<b>Simulation [15]</b>	<b>Current study (SS304L)</b>
<b>Erosion rates [<math>\mu\text{m}^3 \text{ impact}^{-1}</math>]</b>	2.2-5.5		7850

*Appendix 1. Nomenclature*

$b_a$	Anodic Tafel slope. [V decade <sup>-1</sup> ]
$b_c$	Cathodic Tafel slope. [V decade <sup>-1</sup> ]
$C_k$	Cutting characteristic velocity. [m s <sup>-1</sup> ]
$C_p$	Specific heat capacity. [J kg <sup>-1</sup> K <sup>-1</sup> ] (439)
$c_p$	Particle concentration. [kg m <sup>-3</sup> ]
$D$	Diameter of a pipe bore. [m]
$D_k$	Deformation characteristic velocity. [m s <sup>-1</sup> ]
$d_p$	Particle diameter. [m] (0.001)
$\Delta E$	Over potential. [V ]
$E_{app}$	Applied potential. [V ]
$E_e$	Elastic modulus of collision. [Pa]
$E_f$	Deformation erosion factor. [J m <sup>-3</sup> ]
$e_n$	normal coefficient of restitution
$E_p$	Particle Young's modulus. [Pa]
$E_{pas}$	Passivation potential. [V ]
$Er_c$	Cutting Erosion rate. [dimensionless]
$Er_d$	Plastic deformation erosion rate. [dimensionless]
$E_{rev}$	Reversible equilibrium potential. [V ]
$E_t$	Target Young's modulus. [Pa]
$e_t$	tangential coefficient of restitution.
$F$	Faraday number. [C mol <sup>-1</sup> ] (96485)
$ft$	Numerical constant. (0.025)
$h$	Oxide layer thickness. [m]
$h_o$	Thickness of passive layer at passive potential. [m](10 <sup>-9</sup> )
$H_s$	Hardness of material. [Pa]
$i$	Dissolution current density. [A m <sup>-2</sup> ]
$i_o$	Exchange current density. [A m <sup>-2</sup> ]
$k_2$	Material constant. (1398.9)
$K_c$	Corrosion rate. [kg m <sup>-2</sup> s <sup>-1</sup> ]
$\Delta K_c$	Additive effect of erosion influencing the corrosion rate. [k gm <sup>-2</sup> s <sup>-1</sup> ]
$K_{co}$	Pure corrosion rate. [kg m <sup>-2</sup> s <sup>-1</sup> ]
$K_e$	Total erosion rate. [kg m <sup>-2</sup> s <sup>-1</sup> ]
$\Delta K_e$	Synergistic effect of corrosion influencing the erosion rate. [kg m <sup>-2</sup> s <sup>-1</sup> ]
$K_{eo}$	Pure erosion rate. [kg m <sup>-2</sup> s <sup>-1</sup> ]
$K_t$	Total wear. [kg m <sup>-2</sup> s <sup>-1</sup> ]
$M_{Fe}$	Relative atomic mass for Fe. [kg] (0.05585)
$m_p$	Particle mass. [kg]
$m_p$	Particle mass. [kg]
$nc$	Strain hardening coefficient. (0.3)
$R_c$	Radius of the curvature of a pipe. [m]
$R_f$	Roundness factor for the particle. (0.5)
$r_p$	Particle radius. [m]
$T_m$	Target material melting temperature. [K] (1808)
$V_p$	Particle impact velocity. [m s <sup>-1</sup> ]
$Y$	Yield stress of the target material. [Pa]
$z_m$	Number of electrons involved in the dissolution reaction. (2)
$\alpha$	Particle impact angle. [rad]
$\lambda$	Particle shape factor. (0.0 for point mass)
$\mu_f$	Coefficient of friction. (0.3)

$\mu_{fc}$	Critical coefficient of friction.
$\nu_p$	Particle Poisson ratio. (0.23)
$\nu_t$	Target Poisson ratio. (0.3)
$\rho_f$	Density of oxide layer. [ $\text{kg m}^{-3}$ ] (5240)
$\rho_p$	Density of the particle. [ $\text{kg m}^{-3}$ ]
$\rho_p$	particle density. [ $\text{kg m}^{-3}$ ]
$\rho_t$	Density of target. [ $\text{kg m}^{-3}$ ]
$\sigma$	Plastic flow stress of the target material. [Pa]